Enhanced Nonlinear Spectroscopy for Monolayers and Thin Films in Near-Brewster's Angle Reflection Pump-probe Geometry

Jun Nishida, Chang Yan, and Michael D. Fayer*

Department of Chemistry, Stanford University, Stanford, CA, 94305

Email: fayer@stanford.edu Phone: (650) 723-4446

Supplementary Material

A. Incident Angle Dependence of Pump-probe Signal: Calculation

In this section, we derive the pump-probe signal amplitudes for various incident angles as in Figure 1B and 1C. The calculation requires the knowledge of (1) the refractive indices of the two layers defining the interface, and (2) the orientational average and distribution of the vibrational probes transition dipole directions. For the C_{11}-alkylsiloxiane monolayer functionalized with $Re(phen)(CO)_3Cl$ studied here, these parameters were characterized in a previous publication.[1] In the following, we first briefly review those results. Then we provide the form of the nonlinear polarization induced in the sample layer. The induced nonlinear polarization emits the signal fields both toward the reflected and transmitted probe directions. The forms of the signal fields will be provided, based on which the heterodyned signal amplitude can be calculated. While Figure 1B and 1C plot the signal for *p*-polarized pump and probe, we provide the results for the other combinations of polarizations as well.

A1. Orientational Distribution and Third-order Susceptibility $\chi^{(3)}$

In a previous publication,[1] we showed that the observed polarization-selective angle-resolved pump-probe signal was well described with the "wobbling-in-a-cone" model, where the transition dipole moments are wobbling in one of the two kinds of cones; the tilt angles and the cone angles for the two cones were distinct, and the exchange between the two cones was not observed up to ~50 ps, the accessible time window in the experiment.

In the following discussion, θ denotes the out-of-plane polar angle (the angle between the transition dipole moment and the surface normal) and ϕ denotes the in-plane angle of the transition dipole moment. Based on the experimental data,[1] we assume the following distribution of the transition dipole moments: 22% of the molecules are in cone 1 ($a_1 = 0.22$, $\theta_{t,1} = 27°$, $\theta_{c,1} = 43°$) and the other 78% of the molecules are in cone 2 ($a_2 = 0.78$, $\theta_{t,2} = 90°$, $\theta_{c,2} = 7.5°$).

The third-order susceptibility of this monolayer is related to the second-order spherical harmonics correlation functions below, which represent the orientational average, distribution, and dynamics of the head groups.[2] Here, we are interested in the susceptibility for the case where the

pump and the probe pulses are temporarily overlapped, i.e. $t = 0$. For the cone with the tilt angle $\theta_{t,i}$ and the cone angle $\theta_{c,i}$, the spherical harmonics correlation functions are given by[2]

$$\begin{aligned}\left\langle Y_2^0 Y_2^{0*}\right\rangle_i = &\frac{5}{16\pi}\left(3\cos^2\theta_{t,i}-1\right)^2\left[C_1^0(\theta_{c,i})+C_2^0(\theta_{c,i})\right]\\ &+\frac{15}{8\pi}\sin^2\theta_{t,i}\cos^2\theta_{t,i}C_1^1(\theta_{c,i})+\frac{15}{32\pi}\sin^4\theta_{t,i}C_1^2(\theta_{c,i})\end{aligned} \tag{S.1a}$$

$$\begin{aligned}\left\langle Y_2^1 Y_2^{1*}\right\rangle_i = &\frac{15}{8\pi}\sin^2\theta_{t,i}\cos^2\theta_{t,i}\left[C_1^0(\theta_{c,i})+C_2^0(\theta_{c,i})\right]\\ &+\frac{5}{32\pi}\left(2+\cos 2\theta_{t,i}+\cos 4\theta_{t,i}\right)C_1^1(\theta_{c,i})+\frac{5}{16\pi}\sin^2\theta_{t,i}\left(\cos^2\theta_{t,i}+1\right)C_1^2(\theta_{c,i})\end{aligned} \tag{S.1b}$$

$$\begin{aligned}\left\langle Y_2^2 Y_2^{2*}\right\rangle_i = &\frac{15}{32\pi}\sin^4\theta_{t,i}\left[C_1^0(\theta_{c,i})+C_2^0(\theta_{c,i})\right]\\ &+\frac{5}{16\pi}\sin^2\theta_{t,i}\left(\cos^2\theta_{t,i}+1\right)C_1^1(\theta_{c,i})+\frac{5}{8\pi}\left\{\sin^8\frac{\theta_{t,i}}{2}+\cos^8\frac{\theta_{t,i}}{2}\right\}C_1^2(\theta_{c,i})\end{aligned} \tag{S.1c}$$

$$\left\langle Y_2^0\right\rangle_i = \sqrt{\frac{5}{16\pi}}\frac{3\cos^2\theta_{t,i}-1}{2}\cos\theta_{c,i}\left(1+\cos\theta_{c,i}\right) \tag{S.1d}$$

$C_1^0(\theta_{c,i})$, $C_2^0(\theta_{c,i})$, $C_1^1(\theta_{c,i})$ and $C_1^2(\theta_{c,i})$ are functions of the cone angle $\theta_{c,i}$:

$$C_1^0(\theta_{c,i}) = \frac{1}{4}\cos^2\theta_{c,i}\left(1+\cos\theta_{c,i}\right)^2 \tag{S.2a}$$

$$C_2^0(\theta_{c,i}) = \frac{1}{20}\left(4-\cos\theta_{c,i}-6\cos^2\theta_{c,i}-\cos^3\theta_{c,i}+4\cos^4\theta_{c,i}\right) \tag{S.2b}$$

$$C_1^1(\theta_{c,i}) = \frac{1}{5}\left\{2+2\cos\theta_{c,i}\left(1+\cos\theta_{c,i}\right)-3\cos^3\theta_{c,i}\left(1+\cos\theta_{c,i}\right)\right\} \tag{S.2c}$$

$$C_1^2(\theta_{c,i}) = \frac{1}{20}\left\{8-7\cos\theta_{c,i}\left(1+\cos\theta_{c,i}\right)+3\cos^3\theta_{c,i}\left(1+\cos\theta_{c,i}\right)\right\} \tag{S.2d}$$

Because there are two types of cones in the monolayer, the spherical harmonics correlation functions are the weighed-average of the correlation functions arising from the two cones:

$$\left\langle Y_2^0 Y_2^{0*}\right\rangle = a_1\left\langle Y_2^0 Y_2^{0*}\right\rangle_1 + a_2\left\langle Y_2^0 Y_2^{0*}\right\rangle_2 \tag{S.3a}$$

$$\left\langle Y_2^1 Y_2^{1*} \right\rangle = a_1 \left\langle Y_2^1 Y_2^{1*} \right\rangle_1 + a_2 \left\langle Y_2^1 Y_2^{1*} \right\rangle_2 \tag{S.3b}$$

$$\left\langle Y_2^2 Y_2^{2*} \right\rangle = a_1 \left\langle Y_2^2 Y_2^{2*} \right\rangle_1 + a_2 \left\langle Y_2^2 Y_2^{2*} \right\rangle_2 \tag{S.3c}$$

$$\left\langle Y_2^0 \right\rangle = a_1 \left\langle Y_2^0 \right\rangle_1 + a_2 \left\langle Y_2^0 \right\rangle_2 \tag{S.3d}$$

These four correlation functions fully describe the anisotropic part of the third-order susceptibility for all the input polarizations. In the following, $\chi^{(3)}_{\text{aniso},\delta\gamma\beta\alpha}$ corresponds to the anisotropic part of the third-order susceptibility for δ-polarization induced by α-polarized E_1, β-polarized E_2 and γ-polarized E_3. E_1 and E_2 arise from a pump pulse, and E_3 arises from a probe pulse. For the definition of the (X, Y, Z) coordinates, refer to Figure S1. All of the non-zero components of $\chi^{(3)}_{\text{aniso},\delta\gamma\beta\alpha}$ were calculated in ref. 2, and reproduced here as Table S1.

A2. Polarization Induction

As seen in Figure S1, two interactions from the pump pulse and another interaction from the probe pulse induce a third-order polarization $P^{(3)\prime}$ in the sample layer through the third-order

$\left\langle \delta\gamma\beta\alpha \right\rangle_S = \chi^{(3)}_{\text{aniso},\delta\gamma\beta\alpha}$	Spherical Harmonics Representation
$\left\langle XXXX \right\rangle_S, \left\langle YYYY \right\rangle_S$	$\frac{1}{9} - \frac{4}{9}\sqrt{\frac{\pi}{5}}\left\langle Y_2^0 \right\rangle + \frac{4\pi}{45}\left\langle Y_2^{0*} Y_2^0 \right\rangle + \frac{4\pi}{15}\left\langle Y_2^{2*} Y_2^2 \right\rangle$
$\left\langle ZZZZ \right\rangle_S$	$\frac{1}{9} + \frac{8}{9}\sqrt{\frac{\pi}{5}}\left\langle Y_2^0 \right\rangle + \frac{16\pi}{45}\left\langle Y_2^{0*} Y_2^0 \right\rangle$
$\left\langle XXYY \right\rangle_S, \left\langle YYXX \right\rangle_S$	$\frac{1}{9} - \frac{4}{9}\sqrt{\frac{\pi}{5}}\left\langle Y_2^0 \right\rangle + \frac{4\pi}{45}\left\langle Y_2^{0*} Y_2^0 \right\rangle - \frac{4\pi}{15}\left\langle Y_2^{2*} Y_2^2 \right\rangle$
$\left\langle XXZZ \right\rangle_S, \left\langle ZZXX \right\rangle_S, \left\langle YYZZ \right\rangle_S, \left\langle ZZYY \right\rangle_S$	$\frac{1}{9} + \frac{2}{9}\sqrt{\frac{\pi}{5}}\left\langle Y_2^0 \right\rangle - \frac{8\pi}{45}\left\langle Y_2^{0*} Y_2^0 \right\rangle$
$\left\langle XYXY \right\rangle_S, \left\langle YXXY \right\rangle_S, \left\langle XYYX \right\rangle_S, \left\langle YXYX \right\rangle_S$	$\frac{4\pi}{15}\left\langle Y_2^{2*} Y_2^2 \right\rangle$
$\left\langle XZXZ \right\rangle_S, \left\langle ZXXZ \right\rangle_S, \left\langle XZZX \right\rangle_S,$ $\left\langle ZXZX \right\rangle_S, \left\langle YZYZ \right\rangle_S, \left\langle ZYYZ \right\rangle_S, \left\langle YZZY \right\rangle_S,$ $\left\langle ZYZY \right\rangle_S$	$\frac{4\pi}{15}\left\langle Y_2^{1*} Y_2^1 \right\rangle$
Others	0

Table S1. Non-zero tensor components of $\chi^{(3)}_{\text{aniso},\delta\gamma\beta\alpha}$ in spherical harmonics representation, reproduced from Ref. 2.

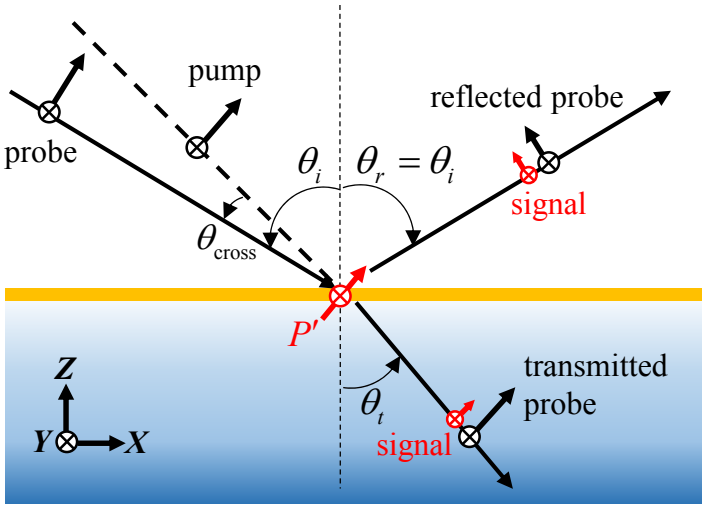

Figure S1. Schematic illustration for pump-probe spectroscopy on an infinitely thin interfacial layer. Any pump and probe polarizations can be decomposed into *p*- and *s*- polarizations. The incident angle θ_i is variable, while the crossing angle θ_{cross} was fixed at 20°. The pump-probe signals can be recorded in either reflection mode or transmission mode.

susceptibility $\chi^{(3)}$. The third-order susceptibility can be decomposed into the isotropic part and the anisotropic part: $\chi^{(3)}_{\delta\gamma\beta\alpha} = \chi^{(3)}_{\text{iso}}\chi^{(3)}_{\text{aniso},\delta\gamma\beta\alpha}$. The isotropic part $\chi^{(3)}_{\text{iso}}$, which includes the phase factor of $\sim i^3$, does not depend on the polarization configurations.

With the third-order susceptibility, the induced polarization $P^{(3)\prime}$ can be obtained as

$$P_X^{(3)\prime} = \sum_{\alpha,\beta,\gamma} \varepsilon_0 \chi_{X\gamma\beta\alpha} (L^{\text{pr}}_{\gamma\gamma} E^{\text{pr}}_{\gamma})(L^{\text{pu}}_{\beta\beta} E^{\text{pu}}_{\beta})(L^{\text{pu}}_{\alpha\alpha} E^{\text{pu}}_{\alpha}) \tag{S.4a}$$

$$P_Y^{(3)\prime} = \sum_{\alpha,\beta,\gamma} \varepsilon_0 \chi_{Y\gamma\beta\alpha} (L^{\text{pr}}_{\gamma\gamma} E^{\text{pr}}_{\gamma})(L^{\text{pu}}_{\beta\beta} E^{\text{pu}}_{\beta})(L^{\text{pu}}_{\alpha\alpha} E^{\text{pu}}_{\alpha}) \tag{S.4b}$$

$$P_Z^{(3)\prime} = \sum_{\alpha,\beta,\gamma} \varepsilon_0 \chi_{Z\gamma\beta\alpha} (L^{\text{pr}}_{\gamma\gamma} E^{\text{pr}}_{\gamma})(L^{\text{pu}}_{\beta\beta} E^{\text{pu}}_{\beta})(L^{\text{pu}}_{\alpha\alpha} E^{\text{pu}}_{\alpha}) \tag{S.4c},$$

where the summation is taken over all the possible 27 combinations of the coordinates, $\{\alpha,\beta,\gamma\} \leftrightarrow \{X,Y,Z\}$. $\vec{\vec{L}}^{\text{pr}}$ and $\vec{\vec{L}}^{\text{pu}}$ are the macroscopic local field correction tensor for the probe field and the pump field.[3, 4] $\vec{\vec{L}}^{\text{pr}}$ is given by

$$L^{\text{pr}}_{XX} = \frac{2n_1 \cos\theta_t}{n_1 \cos\theta_t + n_2 \cos\theta_i} \tag{S.5a}$$

$$L^{\text{pr}}_{YY} = \frac{2n_1 \cos\theta_i}{n_1 \cos\theta_i + n_2 \cos\theta_t} \tag{S5.b}$$

$$L_{ZZ}^{\mathrm{pr}} = \frac{2n_2 \cos\theta_i}{n_1 \cos\theta_t + n_2 \cos\theta_i}\left(\frac{n_1}{n'}\right)^2 \tag{S5.c}$$

Here, θ_i is the incident angle for the probe beam in Figure S1, and θ_t is the refracted transmission angle given by $n_1 \sin\theta_i = n_2 \sin\theta_t$. n' is the refractive index for the sample layer. In our previous report,[1] we showed that it is appropriate to set n' as $n' = \sqrt{n_1^2 + n_2^2 + 4} \Big/ \sqrt{2\left(n_1^{-2} + n_2^{-2} + 1\right)}$.[5, 6] $\vec{\vec{L}}^{\mathrm{pu}}$ can be obtained by replacing θ_i and θ_t in Eqs. (S5.a)-(S5.c) with the incident angle and the transmission angle for the pump beam. The microscopic local field correction factor is assumed to be isotropic and neglected in Eq. (S.4a)-(S.4c).[5, 6]

A3. Signal Emission

The probe beam incident on the layer is partially reflected and partially transmitted. The induced third-order polarization $P^{(3)\prime}$ emits the signal fields both toward the reflected and transmitted probe directions (Figure S1). By solving Maxwell equations with the induced nonlinear polarization, the overall fields emitted toward the reflection direction and the transmission direction can be obtained.[6] Noting that any incident probe field can be decomposed into *p*-polarized ($E_{pr,p}$) and *s*-polarized ($E_{pr,s}$) components, the reflected/transmitted beams for both polarizations can be written as

$$E_{\mathrm{refl},p} = r_p E_{\mathrm{pr},p} + \frac{i\omega}{2c\varepsilon_0 n_1 \cos\theta_i}\left[-L_{XX}^{\mathrm{pr}} P_X' \cos\theta_i + L_{ZZ}^{\mathrm{pr}} P_Z' \sin\theta_i\right] \tag{S.6a}$$

$$E_{\mathrm{refl},s} = r_s E_{\mathrm{pr},s} + \frac{i\omega}{2c\varepsilon_0 n_1 \cos\theta_i} L_{YY}^{\mathrm{pr}} P_Y' \tag{S.6b}$$

$$E_{\mathrm{trans},p} = t_p E_{\mathrm{pr},p} + \frac{i\omega}{2c\varepsilon_0 n_1 \cos\theta_i}\left[\frac{\cos\theta_i}{\cos\theta_t} L_{XX}^{\mathrm{pr}} P_X' \cos\theta_i + \frac{n_1}{n_2} L_{ZZ}^{\mathrm{pr}} P_Z' \sin\theta_i\right] \tag{S.6c}$$

$$E_{\mathrm{trans},s} = t_s E_{\mathrm{pr},s} + \frac{i\omega}{2c\varepsilon_0 n_1 \cos\theta_i} L_{YY}^{\mathrm{pr}} P_Y' \tag{S.6d}$$

where r_p, r_s, t_p and t_s are Fresnel coefficients given by

$$r_p = \frac{n_2 \cos\theta_i - n_1 \cos\theta_t}{n_1 \cos\theta_t + n_2 \cos\theta_i} \tag{S.7a}$$

$$r_s = \frac{n_1 \cos\theta_i - n_2 \cos\theta_t}{n_1 \cos\theta_i + n_2 \cos\theta_t} \tag{S.7b}$$

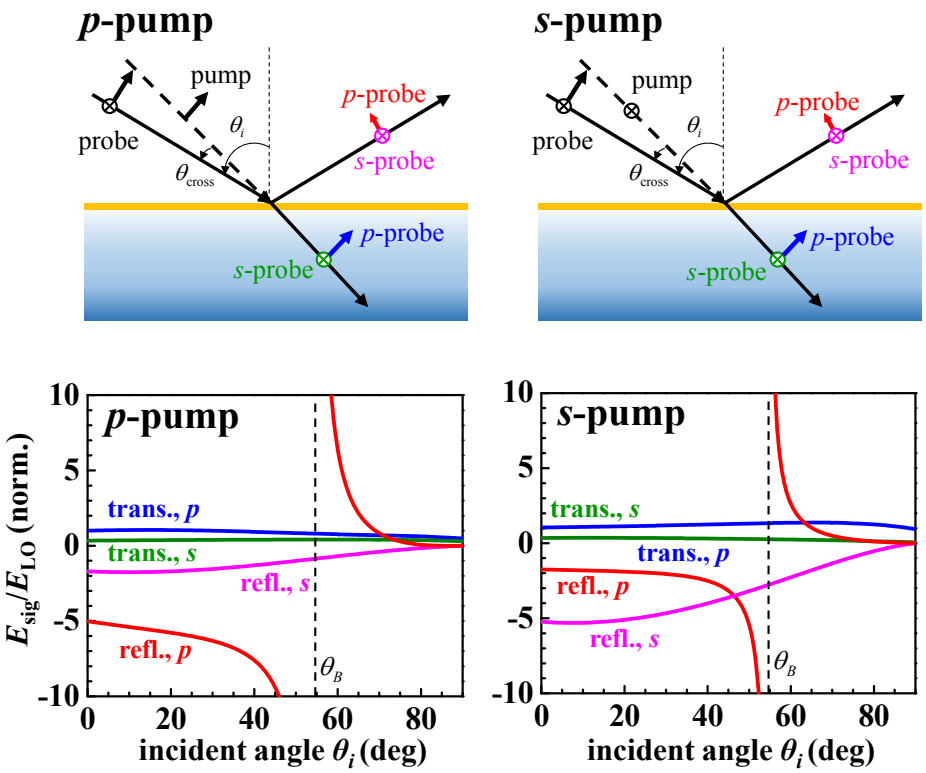

Figure S2. Incident angle θ_i dependence of the pump-probe signal amplitudes for (left) *p*-pump case and (right) *s*-pump case. The four signals in each case arise from the possible combinations of the probe polarizations (*p* or *s*) and the detection mode (reflection or transmission).

$$t_p = \frac{2n_1 \cos\theta_i}{n_1 \cos\theta_t + n_2 \cos\theta_i} \tag{S.7c}$$

$$t_s = \frac{2n_1 \cos\theta_i}{n_1 \cos\theta_i + n_2 \cos\theta_t} \tag{S.7d}$$

The first terms in Eqs. (S.6a)-(S.6d) are the reflected/transmitted probe fields in the absence of the third-order polarization. These first terms are the local oscillator fields, E_{LO}. The second terms in Eqs. (S.6a)-(S.6d) are the third-order signal fields which are emitted from the induced third-order nonlinear polarization. Therefore the amplitude ratio between the second terms and the first terms in Eqs. (S.6a)-(S.6d) are regarded as heterodyned signal amplitudes in each detection mode.

A4. Heterodyned Signal Amplitudes

The heterodyned signal amplitudes calculated for *p*-pump case and *s*-pump case are shown in Figure S2. Note that all the signals are normalized by the *p*-pump and *p*-probe transmission signal with $\theta_i = 0°$. Regardless of the pump polarization, when the probe is *p*-polarized and the

reflected probe is detected, the divergent behavior is observed near Brewster's angle. The other cases do not show this divergent behavior. Among the eight possible polarization and detection configurations, the *p*-polarized pump, *p*-polarized probe signal detected in reflection mode provides the highest heterodyned signal amplitude for the almost entire range of incident angles. This case was experimentally investigated in the main text.

B. Pump-probe Spectroscopy and Two-dimensional Infrared Spectroscopy: Experimental

A regenerative amplifier (Spitfire Ace, Spectra Physics) was seeded with an 83 MHz oscillator output (MaiTai SP, Spectra Physics) and pumped by a Nd:YLF Q-switch laser (Empower, Spectra Physics). The 800 nm regenerative amplifier output (~70 fs, 2 mJ and 3 kHz) was used to pump a home built optical parametric amplifier (OPA). The signal and idler pulses, the outputs from OPA (~500 μJ in total), were temporarily overlapped and collinearly sent to an $AgGaS_2$ crystal (1.5 mm thick) to yield an infrared pulse with ~30 μJ energy, 90 cm^{-1} fwhm band width, and ~190 fs duration. The frequency of the infrared pulse was tuned such that the spectrum is centered at 2025 cm^{-1}. The infrared pulse was split into a strong pump pulse and a weak probe pulse. The pump pulse was sent to a germanium acousto-optic modulator (Ge-AOM) pulse shaping system to shape the temporal profile of the pump pulse. The output from the pulse shaper (~8 μJ) was focused into the sample with an f = 15 cm lens. The probe pulse was focused into the sample with an f = 10 cm lens.

The sample was installed on a rotation stage to control the incident angle of the probe beam (Figure S3). The crossing angle between the pump and the probe beam was set to 20°. The pump and probe pulses' polarizations were set by high-contrast polarizers (ISP Optics, POL-3-5-SI-25; >10000:1 contrast). Either the transmitted or reflected probe beam was sent to a spectrograph to disperse the probe pulse by frequency, and each frequency component (ω_m) of the probe pulse was detected by a 32-pixel HgCdTe array detector. An optical density filter was placed in front of a spectrograph when HgCdTe detector was saturated by a strong probe pulse.

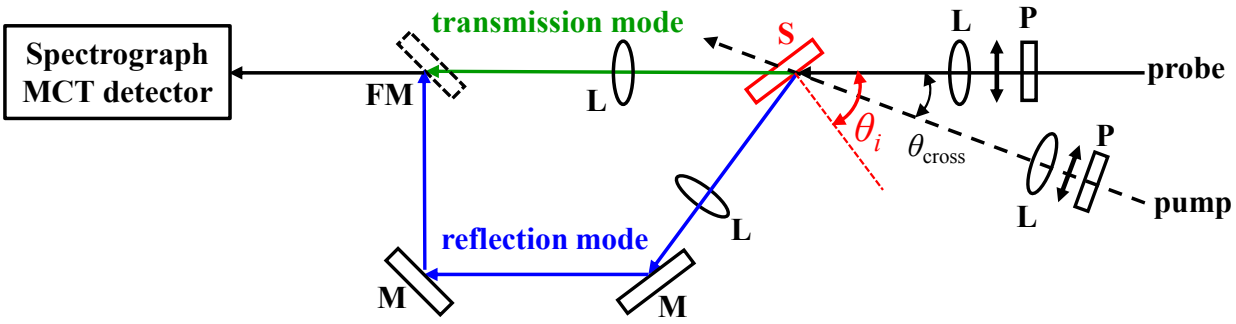

Figure S3. Illustration for the pump-probe experiment setup. P: high contrast polarizers to set the beam polarizations to *p*-polarization, L: focusing or collimating lenses, M: gold mirrors, FM: flip-up mirror; "up" for reflection mode detection and "down" for transmission mode detection, S: sample wafer on a rotation stage. θ_{cross} was set to 20°. θ_i is variable by rotating the sample wafer.

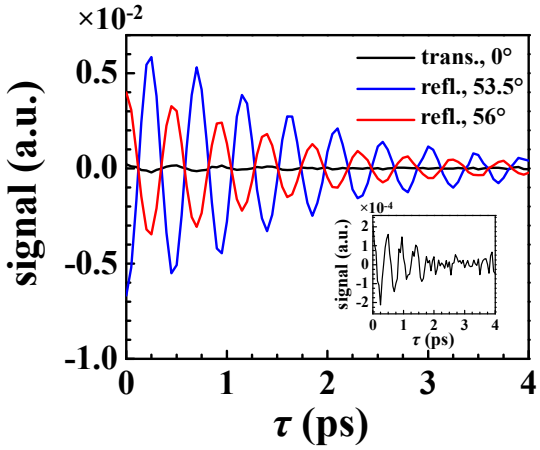

Figure S4. 2D IR interferograms acquired in 5 minutes with different detection modes: transmission mode with normal incidence (black), reflection mode with two different incident angles 53.5° (blue) and 56° (red). The interferograms were recorded at the optical frequency of 2022 cm^{-1}. The waiting time T_w was set to 1 ps. Inset – expanded transmission mode interferogram.

For pump-probe experiment (Figure 2 in the main text), a single pump pulse was generated every other shot as an output from the AOM pulse shaper. The probe pulse intensity recorded with a pump is I_{on}, and the probe pulse intensity without a pump is I_{off}. The pump-probe signal was recorded as $S_{pp} = (I_{on} - I_{off}) / I_{off}$. The phase of the pump pulse was cycled such that the scatter from the substrate is removed from the observed signals.[7]

For 2D IR experiment (Figure 3 in the main text), two pump pulses separated by τ in time were generated using the AOM pulse shaper. The time τ was scanned from 0 ps to 4 ps with 50 fs steps. The phases of the pump pulses were modulated as τ is scanned so that the interferogram is recorded in a rotating frame with the frame frequency of $\omega_f = 1950\,cm^{-1}$. The measurement in the rotating frame reduces the oscillation frequency in the interferogram, which significantly accelerates the data acquisition rate. The probe intensity recorded is denoted as $I(\phi_1, \phi_2)$, where ϕ_1 and ϕ_2 are the phases of E_1 and E_2. The vibrational echo signal was extracted as

$$S_{echo} = \frac{[I(0,0) + I(\pi,\pi)] - [I(\pi,0) + I(0,\pi)]}{[I(0,0) + I(\pi,\pi)] + [I(\pi,0) + I(0,\pi)]} \quad \text{(S.8)}$$

The numerator and denominator in Eq. (S.8) correspond to the heterodyned signal ($\sim E_{sig} E_{LO}$) and the local oscillator intensity ($\sim |E_{LO}|^2$), respectively.

The echo signal in Eq. (S.8) was recorded for all the τ and the interferograms were acquired as in Figure S4. The interferograms were acquired for a range of optical frequencies, ω_m. The interferograms were Fourier transformed to yield the 2D IR spectra as in Figure 3A in the main text. The 2D IR spectra were acquired with various T_ws. The evolution of the band shape was tracked by center line slope (CLS) method.[8, 9]

C. Enhanced Absorption

The monolayer sample studied here was prepared following the procedure previously reported.[10] A conventional transmission FTIR spectrum is shown in Figure S5A. As experimentally demonstrated in many previous reports,[11-13] a linear polarization $P^{(1)}$, which is usually the source of "absorption", can amplify the reflection intensity when $P^{(1)}$ is induced at an interface. Figure S5B shows the probe spectrum reflected from an SiO_2/CaF_2 substrate with and without the sample monolayer present. The incident angle is 53±0.25° for both cases. No pump beam is incident. It can be seen that, in the probe spectrum reflected from the surface with the monolayer, more intensity is reflected around ~2025 cm^{-1} where the strong vibrational resonance is located. When "absorbance" was calculated using these two spectra with and without the sample layer, a "negative absorbance" was observed around ~2025 cm^{-1} (Figure S5C). The optical density is approximately -15 to -20 mOD, which is significantly larger in amplitude than the transmission absorbance of approximately +0.7 mOD.

These counter-intuitive features can be understood in the completely identical manner we described for the enhanced pump-probe signal. The probe beam induces a $P^{(1)}$ polarization, which emits signal fields. In the transmission mode, the emitted signal field is out-of-phase relative to the transmitted probe beam, which is the local oscillator; they destructively interfere and therefore the overall the transmitted field is reduced by the presence of the $P^{(1)}$ polarization. The signal field in the reflection mode is in-phase with the signal field in transmission mode. However, the reflected probe beam is 180° out-of-phase from the transmitted probe beam. Therefore, the signal field in the reflection mode constructively interferes with the reflected probe beam, and the field amplitude is amplified. As the incident angle approaches the Brewster's angle, the reflected probe beam as a local oscillator approaches zero amplitude, while the signal field remains finite. Therefore, near Brewster's angle, the heterodyned signal amplitude diverges and offers a very large enhancement.

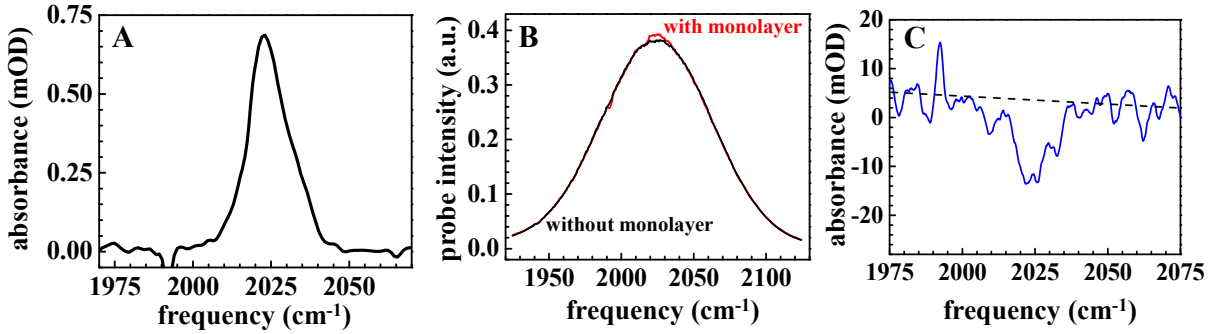

Figure S5. A. Transmission FTIR spectrum of the monolayer acquired with normal incidence. **B.** Spectra of the probe beam reflected from an SiO_2/CaF_2 substrate with (red) and without (black) the monolayer. The spectra were smoothed to enhance the data quality and the black spectrum was scaled such that >2070 cm^{-1} region matches the red spectrum. **C.** Absorbance calculated based on the two spectra in B.

D. Effect of Thickness on the Pump-probe Signal and the Two-dimensional Band Shape

The purpose of this section is to calculate the dependence of the reflection/transmission pump-probe signals on the thickness of the sample layer (Figure 5B in the main text). The approach is based on the method proposed by Hansen,[14] who calculated reflectivity and transmissivity from multi-layers with complex refractive indices, $n_j + ik_j$.

D1. Reflection and Transmission in Three-layer Model

In the following discussion we restrict our interest to *p*-polarized (or TM polarized) probe beam. The discussion below applies regardless of the pump polarization. Hansen explicitly derived the formula for reflection and transmission coefficients in the three-layer model given in Figure S6. For the *p*-polarized probe beam,

$$r = \frac{r_{12} + r_{23}e^{2i\beta}}{1 + r_{12}r_{23}e^{2i\beta}} \tag{S.9a}$$

$$t = \frac{n_1}{n_3}\frac{t_{12}t_{23}e^{i\beta}}{1 + r_{12}r_{23}e^{2i\beta}} \tag{S.9b}$$

The relevant quantities are defined as:

$$r_{jk} = \frac{\hat{\varepsilon}_k\xi_j - \hat{\varepsilon}_j\xi_k}{\hat{\varepsilon}_k\xi_j + \hat{\varepsilon}_j\xi_k} \tag{S.10a}$$

$$t_{jk} = \frac{2\hat{\varepsilon}_k\xi_j}{\hat{\varepsilon}_k\xi_j + \hat{\varepsilon}_j\xi_k} \tag{S.10b}$$

$$\hat{\varepsilon}_j = \hat{n}_j^2 \tag{S.10c}$$

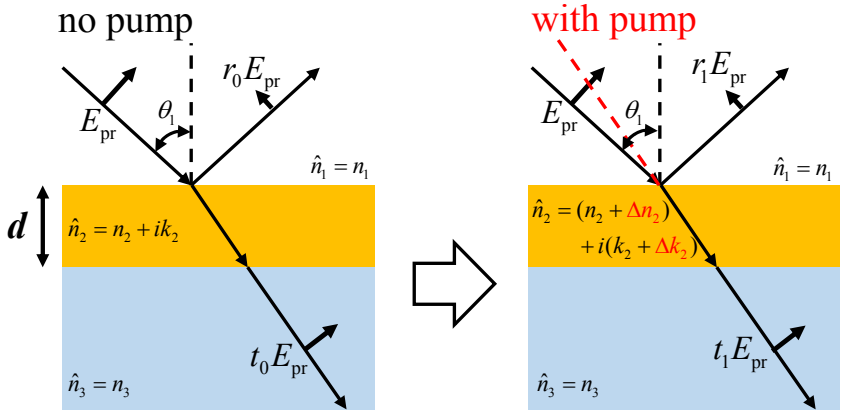

Figure S6. Pump-probe spectroscopy on a layer with finite thickness. The second layer resonantly absorbs the incident IR beams and therefore the refractive index is complex. When the pump beam is incident, the complex refractive index changes. The reflectivity and transmittivity experienced by the probe pulse change accordingly. The changes are detected as the pump-probe signals.

$$\xi_j = \sqrt{\hat{n}_j^2 - n_1^2 \sin^2\theta_1} \tag{S.10d}$$

$$\beta = 2\pi\left(\frac{d}{\lambda}\right)\xi_2 \tag{S.10e}$$

Note that the root in Eq. (S.10d) should be taken so that $\mathrm{Re}[\xi_j] \geq 0$ and $\mathrm{Im}[\xi_j] \geq 0$.

D2. Pump-probe Signal in Reflection and Transmission Mode

The reflection and transmission coefficients, r_0 and t_0, in the absence of the pump pulse can be calculated based on Eqs. (S.9a) and (S.9b) by setting the second layer's refractive index to $\hat{n}_2 = n_2 + ik_2$. With the presence of the pump pulse, the complex refractive index of the second layer changes to $\hat{n}_2 = (n_2 + \Delta n_2) + i(k_2 + \Delta k_2)$, where Δn_2 and Δk_2 are induced by the third-order susceptibility $\chi^{(3)}$ as discussed below. Accordingly the reflection and transmission coefficients change to r_1 and t_1. The observed pump-probe signals for reflection mode (S_{refl}) and transmission mode (S_{trans}) are given by

$$S_{\mathrm{refl}} = \frac{|r_1|^2 - |r_0|^2}{|r_0|^2} \tag{S.11a}$$

$$S_{\mathrm{trans}} = \frac{|t_1|^2 - |t_0|^2}{|t_0|^2} \tag{S.11b}$$

D3. Relationship between (Δn_2, Δk_2) and $\chi^{(3)}$

In the absence of the pump pulse, the refractive index of the second layer and the first-order susceptibility are related by

$$n_2^2 - k_2^2 = 1 + \mathrm{Re}[\chi^{(1)}] \tag{S.12a}$$

$$2n_2k_2 = \mathrm{Im}[\chi^{(1)}] \tag{S.12b}$$

When the pump pulse is incident on the sample, the third-order susceptibility contributes to the complex refractive index:

$$(n_2 + \Delta n_2)^2 - (k_2 + \Delta k_2)^2 = 1 + \mathrm{Re}[\chi^{(1)}] + \mathrm{Re}[\chi^{(3)}] \tag{S.13a}$$

$$2(n_2 + \Delta n_2)(k_2 + \Delta k_2) = \mathrm{Im}[\chi^{(1)}] + \mathrm{Im}[\chi^{(3)}] \tag{S.13b}$$

For $|\chi^{(3)}| \ll 1$, the changes in the refractive indices will be accordingly small, i.e. $\Delta n_2, \Delta k_2 \ll 1$. In this limit, Eqs. (S.13a) and (S.13b) can be linearized to

$$(n_2^2 - k_2^2) + 2(\Delta n_2 - \Delta k_2) = 1 + \mathrm{Re}[\chi^{(1)}] + \mathrm{Re}[\chi^{(3)}] \tag{S.14a}$$

$$2n_2 k_2 + 2n_2 \Delta k_2 + 2k_2 \Delta n_2 = \mathrm{Im}[\chi^{(1)}] + \mathrm{Im}[\chi^{(3)}] \tag{S.14b}$$

Comparing with (S.12a) and (S.12b),

$$2(\Delta n_2 - \Delta k_2) = \mathrm{Re}[\chi^{(3)}] \tag{S.15a}$$

$$2n_2 \Delta k_2 + 2k_2 \Delta n_2 = \mathrm{Im}[\chi^{(3)}] \tag{S.15b}$$

By solving Eqs. (S.15a) and (S.15b) with respect to Δn_2 and Δk_2 with an assumption $k_2 \ll n_2$,

$$\Delta n_2 = \frac{n_2 \,\mathrm{Re}[\chi^{(3)}] + \mathrm{Im}[\chi^{(3)}]}{2n_2} \tag{S.16a}$$

$$\Delta k_2 = \frac{\mathrm{Im}[\chi^{(3)}]}{2n_2} \tag{S.16b}$$

The third-order susceptibility $\chi^{(3)} = \mathrm{Re}[\chi^{(3)}] + i\,\mathrm{Im}[\chi^{(3)}]$ induced by the pump pulse changes the complex refractive index of the second layer through (S.16a) and (S.16b). The change in the complex refractive index induces the change in the reflectivity and the transmittivity (Figure S6), leading to the pump-probe signal in (S.11a) and (S.11b).

As seen above, in general S_{refl} and S_{trans} depend non-linearly on the third-order susceptibility $\chi^{(3)}$. As numerically shown below, if $\left|\chi^{(3)}\right| \ll 1$, S_{refl} and S_{trans} depend linearly on $\mathrm{Re}[\chi^{(3)}]$ and on $\mathrm{Im}[\chi^{(3)}]$. In other words, S_{refl} and S_{trans} can be written as

$$S_{\mathrm{refl}}(\omega_m) = C_{\mathrm{refl}}^{\mathrm{real}}\,\mathrm{Re}[\chi^{(3)}(\omega_m)] + C_{\mathrm{refl}}^{\mathrm{imag}}\,\mathrm{Im}[\chi^{(3)}(\omega_m)] \tag{S.17a}$$

$$S_{\mathrm{trans}}(\omega_m) = C_{\mathrm{trans}}^{\mathrm{real}}\,\mathrm{Re}[\chi^{(3)}(\omega_m)] + C_{\mathrm{trans}}^{\mathrm{imag}}\,\mathrm{Im}[\chi^{(3)}(\omega_m)] \tag{S.17b}$$

where $S_{\mathrm{refl}}(\omega_m)$ and $S_{\mathrm{trans}}(\omega_m)$ are the pump-probe signals in reflection/transmission modes at each optical frequency ω_m.

Figure 5B in the main text plots $C_{\mathrm{refl}}^{\mathrm{real}}, C_{\mathrm{refl}}^{\mathrm{imag}}, C_{\mathrm{trans}}^{\mathrm{real}}$ and $C_{\mathrm{trans}}^{\mathrm{imag}}$ in Eqs. (S.17a) and (S.17b) with respect to the sample thickness. For the transmission mode, $C_{\mathrm{trans}}^{\mathrm{real}}$ is negligibly small compared with $C_{\mathrm{trans}}^{\mathrm{imag}}$ and therefore the band shape is purely absorptive ($\propto \mathrm{Im}[\chi^{(3)}(\omega_m)]$). For the

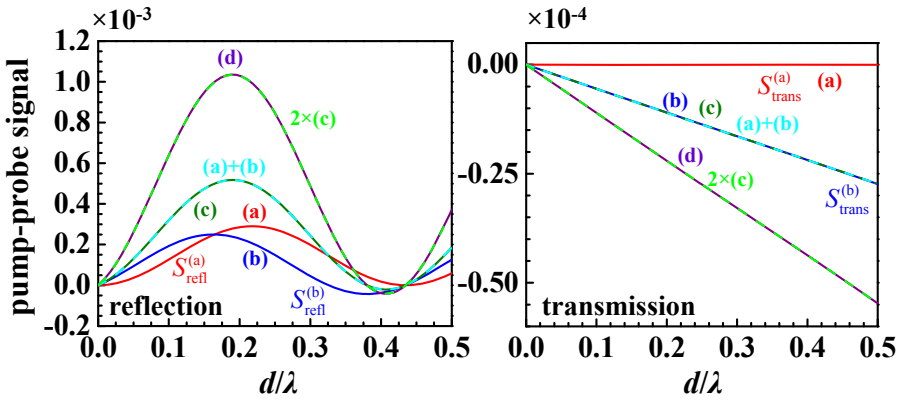

Figure S7. Reflection (left) and transmission (right) pump-probe signals induced by $\chi^{(3)}$ of (a) 10^{-5}, (b) $10^{-5}i$, (c) $10^{-5} + 10^{-5}i$, and (d) $2\times10^{-5} + 2\times10^{-5}i$. (a)+(b) and 2×(c) are plotted as well, verifying that the pump-probe signal linearly depend on $\chi^{(3)}$ as in Eqs. (S.17) for the small $\chi^{(3)}$ of ~10^{-5}.

reflection mode, depending on the thickness, $C_{\text{refl}}^{\text{real}}$ is not negligible and therefore the dispersive band shape ($\propto \text{Re}[\chi^{(3)}(\omega_m)]$) significantly affects the 2D IR band shape $S_{\text{refl}}(\omega_m)$.

D4. Numerical Proof for Eqs. (S.17a) and (S.17b)

S_{refl} and S_{trans} were calculated for the layers in Figure 5A with various $\chi^{(3)}$ and plotted in Figure S7. For the plots in Figure S7, the infinitesimally small absorption by the layer is assumed, i.e. $k_2 \to 0$. For the small $\left|\chi^{(3)}\right|$ on the order of ~10^{-5}, the linearity in Eqs. (S.17a) and (S.17b) is verified as seen in Figure S7. For example, $S_{\text{refl.}}^{(\text{a})}$ was calculated with $\chi^{(3)} = 10^{-5}$, while $S_{\text{refl.}}^{(\text{b})}$ was calculated with $\chi^{(3)} = 10^{-5}i$. When the pump-probe signal with $\chi^{(3)} = 10^{-5} + 10^{-5}i$ was calculated (the curve (c) in Figure S7), the signal amplitude is well-approximated as $S_{\text{refl.}}^{(\text{a})} + S_{\text{refl.}}^{(\text{b})}$.

Based on Figure S7, $C_{\text{refl}}^{\text{real}}$, $C_{\text{refl}}^{\text{imag}}$, $C_{\text{trans}}^{\text{real}}$ and $C_{\text{trans}}^{\text{imag}}$ can be obtained as

$$C_{\text{refl}}^{\text{real}} = S_{\text{refl.}}^{(\text{a})} / 10^{-5} \tag{S.18a}$$

$$C_{\text{refl}}^{\text{imag}} = S_{\text{refl.}}^{(\text{b})} / 10^{-5} \tag{S.18b}$$

$$C_{\text{trans}}^{\text{real}} = S_{\text{trans.}}^{(\text{a})} / 10^{-5} \tag{S.18c}$$

$$C_{\text{trans}}^{\text{imag}} = S_{\text{trans.}}^{(\text{b})} / 10^{-5} \tag{S.18d}$$

These are plotted in Figure 5B with respect to the layer's thickness.

D5. Calculation of Two-dimensional Band Shape

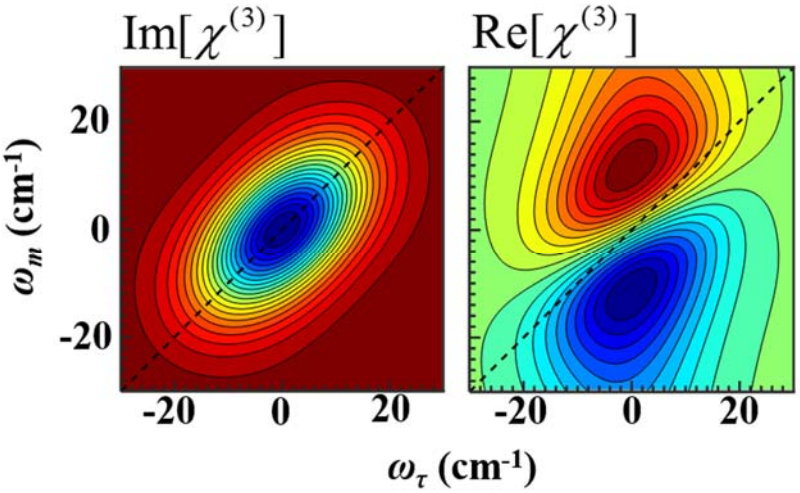

Figure S8. Im[$\chi^{(3)}$] (left, absorptive) and Re[$\chi^{(3)}$] (right, dispersive) 2D band shapes calculated based on the FFCF given in Eq. (S.19). The waiting time T_w was set to 15 ps. The observed 2D IR signals in reflection/transmission modes can be expressed as the superposition of these two band shapes as in Eqs. (S.17).

The frequency-domain third-order susceptibility $\chi^{(3)}(\omega_\tau, T_w, \omega_m)$ was obtained by Fourier transforming the time-domain response function $R^{(3)}(t_1, T_w, t_3)$ with respect to t_1 and t_3. Care needs to be paid in terms of the definition of a response function; $\{iR^{(3)}(t_1, T_w, t_3)\}^*$ instead of $R^{(3)}(t_1, T_w, t_3)$ is often referred to as a response function. While $R^{(3)}(t_1, T_w, t_3)$ is proportional to an induced third-order polarization, $\{iR^{(3)}(t_1, T_w, t_3)\}^*$ is proportional to an emitted third-order signal field and thus is 90° phase-shifted from a nonlinear polarization. For example in ref. 8, $\{iR^{(3)}(t_1, T_w, t_3)\}^*$ is called a response function. The definition of the response function must be carefully tracked to accurately obtain the band shape and its sign.

When the frequency-frequency correlation function (FFCF) is provided, the time-domain response function $R^{(3)}(t_1, T_w, t_3)$ can be calculated. The formula is given in ref. 8. As mentioned in the main text, we used

$$\left\langle \delta\omega(0)\delta\omega(t) \right\rangle = \delta(t)/(3\,\text{ps}) + (10\ \text{cm}^{-1})^2 \times \exp\left[-t/(30\,\text{ps})\right] \tag{S.19}$$

as an FFCF to simulate $\chi^{(3)}(\omega_\tau, T_w, \omega_m)$. The real and imaginary parts of the simulated $\chi^{(3)}$ are shown in Figure S8 for T_w = 15 ps. As seen in Eqs. (S.17a) and (S.17b), the observed signals are superposition of these two band shapes. $C_{\text{refl}}^{\text{real}}$, $C_{\text{refl}}^{\text{imag}}$, $C_{\text{trans}}^{\text{real}}$ and $C_{\text{trans}}^{\text{imag}}$ were all calculated above. The signal band shapes in reflection/transmission modes can thus be constructed based on Eqs. (S.17a) and (S.17b). The results were plotted in Figure 5B in the main text.

References

1. J. Nishida, C. Yan, and M. D. Fayer, J. Am. Chem. Soc. **138**, 14057 (2016).

2. J. Nishida, and M. D. Fayer, J. Chem. Phys. **140**, 144702 (2014).
3. Y. Shen, Annu. Rev. Phys. Chem. **40**, 327 (1989).
4. T. F. Heinz, Nonlinear Surface Electromagnetic Phenomena **29**, 353 (1991).
5. X. Zhuang, P. B. Miranda, D. Kim, and Y. R. Shen, Phys. Rev. B **59**, 12632 (1999).
6. S. Yamaguchi, H. Hosoi, M. Yamashita, P. Sen, and T. Tahara, J. Phys. Chem. Lett. **1**, 2662 (2010).
7. S.-H. Shim, and M. T. Zanni, Phys. Chem. Chem. Phys. **11**, 748 (2009).
8. K. Kwak, S. Park, I. J. Finkelstein, and M. D. Fayer, J. Chem. Phys. **127**, 124503 (2007).
9. K. Kwak, D. E. Rosenfeld, and M. D. Fayer, J. Chem. Phys. **128**, 204505 (2008).
10. D. E. Rosenfeld, Z. Gengeliczki, B. J. Smith, T. D. P. Stack, and M. D. Fayer, Science **334**, 634 (2011).
11. R. A. Dluhy, J. Phys. Chem. **90**, 1373 (1986).
12. H. Brunner, U. Mayer, and H. Hoffmann, Appl. Spectrosc. **51**, 209 (1997).
13. Y. Nishikawa, K. Fujiwara, K. Ataka, and M. Osawa, Anal. Chem. **65**, 556 (1993).
14. W. N. Hansen, J. Opt. Soc. Am. **58**, 380 (1968).